

Global Unifying Intrinsic Calibration for Spinning and Solid-State LiDARs

Jiunn-Kai Huang, Chenxi Feng, Madhav Achar, Maani Ghaffari, and Jessy W. Grizzle

Abstract—Sensor calibration, which can be intrinsic or extrinsic, is an essential step to achieve the measurement accuracy required for modern perception and navigation systems deployed on autonomous robots. Intrinsic calibration models for spinning LiDARs have been based on hypothesized physical mechanisms, resulting in anywhere from three to ten parameters to be estimated from data, while no phenomenological models have yet been proposed for solid-state LiDARs. Instead of going down that road, we propose to abstract away from the physics of a LiDAR type (spinning vs. solid-state, for example) and focus on the point cloud’s spatial geometry generated by the sensor. By modeling the calibration parameters as an element of a matrix Lie Group, we achieve a unifying view of calibration for different types of LiDARs. We further prove mathematically that the proposed model is well-constrained (has a unique answer) given four appropriately orientated targets. The proof provides a guideline for target positioning in the form of a tetrahedron. Moreover, an existing semi-definite programming global solver for SE(3) can be modified to efficiently compute the optimal calibration parameters. For solid-state LiDARs, we illustrate how the method works in simulation. For spinning LiDARs, we show with experimental data that the proposed matrix Lie Group model performs equally well as physics-based models in terms of reducing the point-to-plane distance while being more robust to noise.

I. INTRODUCTION

Camera and Light Detection And Ranging (LiDAR) sensors and supporting software are common system elements in current robotic and autonomous systems. For real-world operation, such systems’ performance depends on the quality of intrinsic and extrinsic calibration parameters. Intrinsic calibration of a sensor is the process of ensuring that obtained measurements are meaningful and valid. Intrinsic calibration of cameras is relatively mature [1]–[3] and many open-source packages are available [4]–[6]. Similarly, intrinsic calibration is also required for LiDARs; otherwise, the obtained point clouds are potentially inaccurate. However, even though spinning LiDARs have been on the market for over ten years, no publication supported by open-source calibration software is currently available, forcing academic researchers to either spend time developing their own solutions or to ignore concerns about the accuracy of their LiDAR point clouds.

Recently, another type of LiDAR, solid-state LiDAR, is being brought to the market. Industry is turning to solid-state LiDARs because they are small, quiet and produce less vibration. Due to their small size, they can be nicely integrated with headlights or carried by mobile robots such

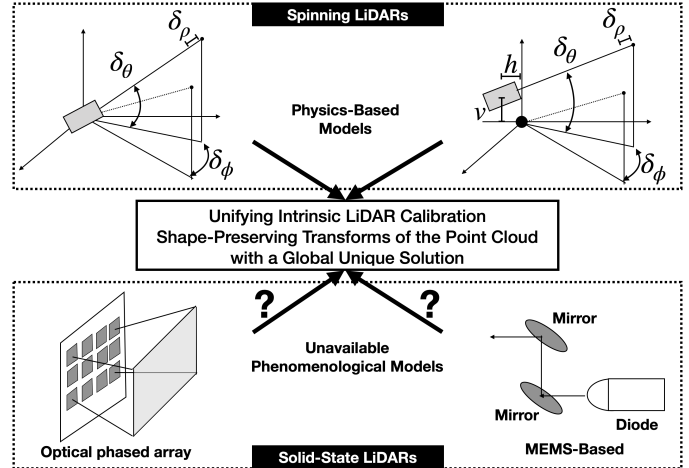


Fig. 1: Is it possible to calibrate a LiDAR without modeling the physical mechanism itself? This paper says YES it is and it allows a unifying means to calibrate LiDARs of all types. Top left: shows a simple physics-based calibration model for a spinning LiDAR. Top right: shows a similar model with more parameters, also for a spinning LiDAR. In the literature, the number of parameters can vary from three to ten. Bottom left and bottom right show, respectively, an optical phased array solid-state LiDAR and a MEMS-based solid-state LiDAR. There are many design options and many manufacturing steps to fabricate these LiDARs. This paper moves the attention to the geometry of the LiDAR’s point cloud and proposes that calibration can be achieved via shape-preserving transformations.

as drones. Moreover, solid-state LiDARs are more reliable especially for automotive applications due to the absence of the rotating mechanism. Because spinning LiDARs have a relatively simple working mechanism, it has been possible to propose physics-based calibration models [7]–[14], see Sec. II-A. For solid-state LiDARs, however, multiple types and design options are being proposed (see Sec. II-B), and thus it is going to be difficult to hand-craft a calibration model for each design of a solid-state LiDAR. We ask, is it necessary to do this? Are type-specific calibration models even the right way to approach the problem?

In this work, we propose a unifying view of calibration for different types of LiDARs, as shown in Fig. 1: we tie the calibration process to the data produced by the sensor, and not the sensor itself, by applying shape-preserving transformations to a LiDAR’s point cloud. Additionally, we prove mathematically that the proposed calibration model is well-constrained (i.e., a unique answer exists), whereas existing physics-based calibration models do not guarantee a unique set of calibration parameters. The uniqueness proof for the proposed method provides a guideline for target positioning. In addition, uniqueness of the parameters is necessary if one is to investigate a globally convergent parameter solver.

The authors are with the Robotics Institute, University of Michigan, Ann Arbor, MI 48109, USA. {bjhuang, chenxiF, achar, maanigj, grizzle}@umich.edu.

A. Our Contributions

- 1) We propose a model for intrinsic LiDAR calibration that is independent of the underlying technology. The new error model is based on shape-preserving transformations¹, which is a rigid body transformation plus a scale factor. Currently, intrinsic calibration models have been published for spinning LiDARs, while for solid-state LiDARs, the calibration models used by manufacturers have not found their way into the published literature. Current calibration models are tied to postulated physical mechanisms for how a LiDAR functions, resulting in anywhere from three to ten parameters to be estimated from data. Instead, we *abstract away from the physics of a LiDAR type* (spinning head vs. solid-state, for example) and focus on the spatial geometry of the point cloud generated by the sensor. *This leads to a unifying view of calibration* and results in an error model that can be represented as the action of the seven-dimensional matrix Lie group, $Sim(3)$, on subsets of the measurements returned by the LiDAR.
- 2) One may suspect that our proposed model is over-parameterized. We, therefore, mathematically prove that given four targets with appropriate orientations, the proposed model is well-constrained (i.e., only one answer exists). The proof provides a guideline for target placement, which is an oriented tetrahedron.
- 3) We give a globally convergent means to determine the calibration parameters. It utilizes an alternating optimization technique to solve the calibration problem, where the scaling parameter is determined by the bisection method, and the rest of the parameters ($SE(3)$) are formulated as a Quadratically Constrained Quadratic Program (QCQP) where the Lagrangian dual relaxation is used. The relaxed problem on $SE(3)$ becomes a Semidefinite Program (SDP) and convex [15]–[18]. Therefore, the calibration problem can be solved globally and efficiently by off-the-shelf solvers [19].
- 4) We provide a MATLAB-based simulator for intrinsic LiDAR calibration and validation that allows one to study the effects of target placement and the effectiveness of various calibration methods.
- 5) In simulations, we validate that positioning the four targets as a tetrahedron can calibrate equally well a spinning LiDAR and a solid-state LiDAR. In experiments on a spinning LiDAR, we show that the proposed method works as well as two physics-based models in terms of Point-to-Plane (P2P) distance, while it is more robust when we induce systematic errors to the experimental measurements.
- 6) We open-source all of the related software for intrinsic calibration, including implementations of the baseline methods, the simulator, the data sets and the solver; see [20]–[22].

II. RELATED WORK

This section overviews related work as well as spinning and solid-state LiDARs.

¹Called *similarity transformations* in projective geometry.

A. Spinning LiDAR

A spinning LiDAR as used in this paper consists of K laser emitter-receiver pairs mounted at various positions and elevation angles on a rotating head, as shown in Fig. 1. The lasers are pulsed at a fixed frequency. Each revolution of the rotating head sweeps out a cone in space, called a LiDAR scan, composed of discrete return points traced out by each pulsed emitter-receiver. The points associated with a single laser beam are called a ring.

The measurements are typically viewed as being made in a spherical coordinate system. The range measurement is made by estimating time-of-flight (ToF) through a clocking system on a circuit board, the azimuth is estimated from the position of the rotating head, and the elevation angle of a beam is determined by its mounting angle on the rotating head.

Existing error models for LiDARs are phenomenological in nature, that is, they are tied to physical explanations of a sensor’s design and/or operation [7]–[14]. Broadly speaking, two common sources of uncertainty considered in spinning LiDAR models are (1) errors in the clocking systems, (one for ToF and one for pulsing the lasers) and (2) mechanical errors associated with positioning of the beams on the spinning LiDAR. Less commonly considered are affects are due to ambient temperature or target size. Some authors overlook that the measurements are actually made in a local coordinate frame for each emitter-receiver pair, and are then transformed to a single “global” frame for the LiDAR unit, resulting in models with three to six parameters [8], [9], [13], while others take this into account and use as many as ten parameters [14]. Moreover, none of these models provides a guideline for target placement so that the calibration model is well-constrained (i.e., a unique solution exists), see Sec. III-D.

B. Solid-State LiDAR

In comparison to spinning LiDARs, solid-state LiDARs are smaller, quieter, lower-cost, and produce less vibration. Several types of solid-state LiDAR are coming to the market, including those based on (1) Optical Phased Array (OPA) [23]–[25], and (2) Micro-Electro-Mechanical System (MEMS) mirrors² [26]–[31].

OPA-based solid-state LiDARs function similarly to a phased array in antenna theory. A single OPA contains a significant number of emitters patterned on a chip. By varying the phase shift (i.e., time delay) of each emitter, the direction of the resulting wave-front or the spread angle can be adjusted. In particular, the sensor is able to zoom in or out of an object on command. On the other hand, MEMS-based solid-state LiDARs use only one or a few emitters, with the beams guided by a mirror system regulated by a sophisticated controller. The controller seeks to steer the beam (or beams) in a scanning pattern, such as a zig-zag [26].

To perfectly align OPA emitters or MEMS mirrors is challenging. It is also hard to maintain high accuracy under different temperatures and weather conditions. Thus, how to properly calibrate a solid-state LiDAR is a critical problem.

²Some authors argue MEMS-based solid-state LiDARs are not truly solid-state devices due to the movable mirrors; the mirrors, however, are tiny compared to a spinning LiDAR.

The variety of solid-state LiDARs raises the question: is it necessary, or even possible, to design/create parameterized models for every type of solid-state LiDAR? This paper seeks to present a unifying view of LiDAR calibration by abstracting away from the physics of a LiDAR type (spinning vs solid state, for example), and focusing instead on the spatial geometry of the point cloud generated by the sensor. This leads to a unifying view of calibration.

III. PROPOSED LiDAR INTRINSIC MODEL AND ANALYSIS

The proposed calibration parameters are modeled as an element of the similarity Lie group $\text{Sim}(3)$, which can be applied to both spinning LiDARs and solid-state LiDARs. An element of the group is an isometry composed with an additional isotropic scaling, i.e., a rigid-body transformation with scaling. We note that this is the most general form of a shape-preserving transformation in 3D space (i.e. preserves ratios of lengths and angles). We also note that (8) and (9) are not shape preserving. It will be important to see in real data if our assumption of shape preservation is general enough to provide useful calibrations.

An element of the group is given by

$$\mathbf{H} = \begin{bmatrix} s\mathbf{R} & \mathbf{v} \\ \mathbf{0} & 1 \end{bmatrix} \in \text{Sim}(3), \quad (1)$$

where $\mathbf{R} \in \text{SO}(3)$ is the 3D rotation matrix, $\mathbf{v} \in \mathbb{R}^3$ is the translation vector, and $s \in \mathbb{R}^+$ is the scale parameter. In particular, an element has seven degrees of freedom and the action of $\text{Sim}(3)$ on \mathbb{R}^3 is $\mathbf{H} \cdot \mathbf{x} = s\mathbf{R}\mathbf{x} + \mathbf{v}$, where $\mathbf{x} \in \mathbb{R}^3$ and where $\mathbf{H} \cdot \mathbf{x}$ uses homogeneous coordinates while $s\mathbf{R}\mathbf{x} + \mathbf{v}$ uses Cartesian coordinates. From hereon, wherever convenient, we abuse notation by passing from regular coordinates to homogeneous coordinates without noting the distinction.

A. Point-to-Plane Distance

Let \mathbf{n}_t be a unit normal vector of a planar target and let $\mathbf{p}_{0,t}$ be a fixed point on the target. Let $\mathcal{X} = \{\mathbf{x}_i | i = 1, \dots, M \text{ and } \mathbf{x}_i \in \mathbb{R}^3\}$ denote a collection of LiDAR returns on the target, and M be the number of points in the collection. Given the collection of LiDAR returns \mathcal{X} , the cost of the intrinsic calibration problem is commonly defined by the P2P distance:

$$J_t := \sum_{i=1}^M J_i(\mathbf{x}_i, \mathbf{n}_t, \mathbf{p}_{0,t}) := \sum_{i=1}^M (\mathbf{n}_t^\top (\mathbf{x}_i - \mathbf{p}_{0,t}))^2, \quad (2)$$

where $\mathbf{n}_t^\top (\mathbf{x}_i - \mathbf{p}_{0,t})$ is the orthogonal projection of the measurement onto the normal vector. Then the calibration problem can be formulated as follows

Problem 1. For a given collection of points $\mathcal{X}_t = \{\mathbf{x}_i\}_{i=1}^{M_t}$, possibly from multiple targets $t \in \{1, \dots, T\}$, we seek a similarity transformation \mathbf{H}^* that solves

$$\min_{\mathbf{H} \in \text{Sim}(3)} \sum_{t=1}^T \sum_{i=1}^{M_t} (\mathbf{n}_t^\top (\mathbf{H} \cdot \mathbf{x}_i - \mathbf{p}_{0,t}))^2. \quad (3)$$

Remark 1. The transformation H applies to the entire collection of points \mathcal{X} . How to define the collection is addressed in Sec. III-B.

Remark 2. In practice each target's normal vector and a point on the target must be estimated from data; see [32], [33].

B. Parsing Points on a Target to Collections of Points

The specific method for parsing a target's point cloud and the number of calibration transformations depends on the nature of the sensor. For a spinning LiDAR, the points \mathcal{PC} on a target are typically separated by beam number so each beam has its own optimization problem (3). For example, for a K -beam spinning LiDAR, a natural choice for the set of calibration parameters is $\{\mathbf{H}_k | k = 1, \dots, K \text{ and } \mathbf{H}_k \in \text{Sim}(3)\}$, where H_k is the similarity transform for the k -th ring. Similarly, one could also split each ring into quarter circles (90° arcs), which would lead to $4K$ calibration parameters. On the one hand, for an OPA-based solid-state LiDAR, we propose to form an $m \times n$ grid over the planar target and then parse the point cloud based on each point's projection onto the target along the normal of each grid. This way, the set of calibration parameters becomes $\{\mathbf{H}_k | k = 1, \dots, m \times n \text{ and } \mathbf{H}_k \in \text{Sim}(3)\}$. On the other hand, one may wish to stick with parsing via "rows or columns". In the end, it's a choice that has to be made by the calibrator.

C. Overfitting, Underfitting, and Model Mismatch

We first point out that the proposed calibration model can suffer from overfitting (i.e., a unique \mathbf{H}^* does not exist) if less than four targets are used to calibrate a LiDAR. In particular, for a single planar target, the rotation about the target normal \mathbf{n}_t , two components of the translation vector \mathbf{v} (translation in the plane of the target), and the scale s are unconstrained. For two planar targets, translation along the line orthogonal to the targets' normal vectors and scale are unconstrained. Therefore, understanding how target positioning constrains the calibration model is essential. As mentioned above, underfitting could occur if the data is parsed into rings, but say one of the rings has distance errors that vary with rotation angle. In this case, splitting each ring into different arcs will eliminate the underfitting.

Our calibration model is not a phenomenological model. The existing published models postulate how a LiDAR works and hence are phenomenological models. These postulated models result in different numbers of parameters, ranging from three to eight. Our "calibration model" abstracts away from the physical device and focuses on transforming the point cloud so that the (x, y, z) values are correct.

D. Target Placement Guideline

Theorem 1 given below provides practically realizable conditions under which a unique answer exists to Problem 1. The proof is given in Appendix A in [34]. We further propose a method to globally compute the unique solution, see Sec. V.

For a subset $\mathcal{S} \subset \mathbb{R}^3$, let $[\mathcal{S}]$ and $[\mathcal{S}]^\perp$ denote its span and its orthogonal complement, respectively. Let $\{\mathbf{e}_1, \mathbf{e}_2, \mathbf{e}_3\}$ be the canonical basis for \mathbb{R}^3 . We also denote $\mathbf{P} \subset \mathbb{R}^3$ a set traced out by a single ring (i.e., a ring plane) of a perfectly calibrated spinning LiDAR. Without loss of generality, we assume $\mathbf{P} = [\mathbf{e}_3]^\perp$.

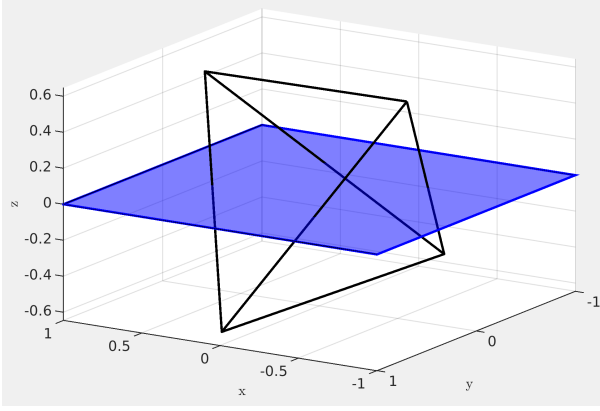


Fig. 2: An oriented tetrahedron (black) and a ring plane (blue) for target positioning that satisfies the conditions of Theorem 1.

Consider four targets with unit normal vectors \mathbf{n}_i and let $\mathbf{p}_{0,i}$ be a point on the i -th target. For $1 \leq i \leq 4$, the plane defined by the i -th target is

$$\begin{aligned} \mathbf{V}_i &:= \mathbf{p}_{0,i} + [\mathbf{n}_i]^\perp \\ &:= \mathbf{p}_{0,i} + \{v \in \mathbb{R}^3 \mid \mathbf{n}_i^\top v = 0\}, \end{aligned}$$

the plane formed by the set of vectors orthogonal to the normal vector \mathbf{n}_i , and subsequently translated by $\mathbf{p}_{0,i}$.

Assumption N (Normal Vectors)

All sets of three distinct vectors from $\{\mathbf{n}_1, \mathbf{n}_2, \mathbf{n}_3, \mathbf{n}_4, \mathbf{e}_3\}$ are linearly independent.

Under Assumption N, for each $i \neq j \in \{1, 2, 3, 4\}$, there exist unique points $\mathbf{p}_{ij} := \mathbf{P} \cap \mathbf{V}_i \cap \mathbf{V}_j$. All total, there are $\binom{4}{2} = 6$ such intersection points.

Assumption B (Basis Vectors)

Each of the following sets of vectors³ is a basis of the ring plane:

- (a) $\{\mathbf{p}_{12}, \mathbf{p}_{13}\}, \{\mathbf{p}_{13}, \mathbf{p}_{14}\}, \{\mathbf{p}_{14}, \mathbf{p}_{12}\},$
- (b) $\{\mathbf{p}_{12}, \mathbf{p}_{23}\}, \{\mathbf{p}_{23}, \mathbf{p}_{24}\}, \{\mathbf{p}_{24}, \mathbf{p}_{12}\},$
- (c) $\{\mathbf{p}_{13}, \mathbf{p}_{23}\}, \{\mathbf{p}_{23}, \mathbf{p}_{34}\}, \{\mathbf{p}_{34}, \mathbf{p}_{13}\},$
- (d) $\{\mathbf{p}_{14}, \mathbf{p}_{24}\}, \{\mathbf{p}_{24}, \mathbf{p}_{34}\}, \{\mathbf{p}_{34}, \mathbf{p}_{14}\},$
- (e) $\{\mathbf{p}_{14}, \mathbf{p}_{23}\}$

We note that for a perfectly calibrated LiDAR, if \mathbf{H} is the identity element of $\text{SE}(3)$, then for all $i \neq j \in \{1, 2, 3, 4\}$, it must be true that $\mathbf{H} \cdot \mathbf{p}_{ij} \in \mathbf{V}_i \cap \mathbf{V}_j$. The following shows that the converse is true when the targets are appropriately positioned and oriented.

Theorem 1. Assume that Assumptions N and B hold and let $\mathbf{H} \in \text{Sim}(3)$. If for each $i \neq j \in \{1, 2, 3, 4\}$, $\mathbf{H} \cdot \mathbf{p}_{ij} \in \mathbf{V}_i \cap \mathbf{V}_j$, then

$$\mathbf{H} = \begin{bmatrix} \mathbf{I} & \mathbf{0} \\ \mathbf{0} & 1 \end{bmatrix}. \quad (4)$$

Proof: See Appendix A in [34].

An immediate Corollary of Theorem 1 is the uniqueness of the transformation, as stated below.

³There are $\binom{6}{2} = 15$ possible pairs of vectors, of which we use 13 to establish uniqueness.

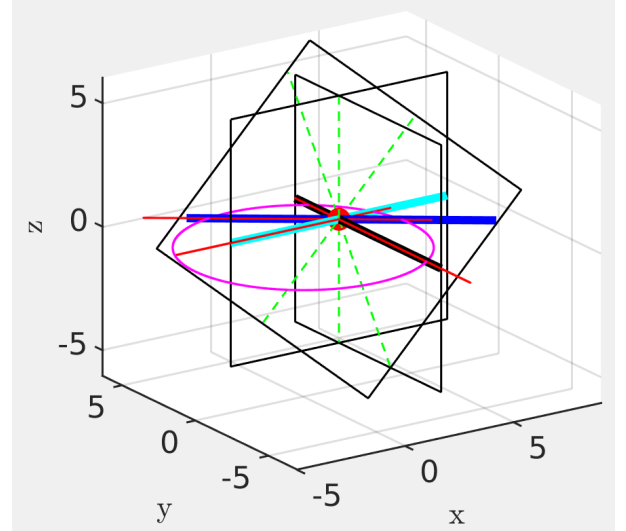


Fig. 3: Illustration of a degenerate case. The black squares are different planes with the normal vectors being linearly independent. The dotted green lines indicate the intersection of two planes. The magenta circle shows the LiDAR ring passing through q_0 (red center bullet) in (5). The thick blue, cyan and black lines are the intersections of the ring planes and the targets. The P2P cost of the intersections are therefore zero. The red lines show the results of applying a transformation $\mathbf{H} = \begin{bmatrix} s\mathbf{I} & (1-s)\mathbf{q}_0 \\ \mathbf{0} & 1 \end{bmatrix}$ to the intersection lines. The cost remains zero because the transformed lines stay on the targets.

Corollary. Let $\tilde{\mathbf{H}} \in \text{Sim}(3)$ and define $\tilde{\mathbf{p}}_{ij} := \tilde{\mathbf{H}}(\mathbf{p}_{ij})$. Then under Assumptions N and B, the only element $\mathbf{G} \in \text{Sim}(3)$ satisfying $\mathbf{G}(\tilde{\mathbf{p}}_{ij}) \in \mathbf{V}_{ij}$ all $i \neq j$ is $\mathbf{G} = \tilde{\mathbf{H}}^{-1}$.

Assumption N assumes linear independence ($\binom{5}{3} = 10$) for any three of the target normal vectors, but does not directly address their “degree of independence,” that is, their condition number. Similarly, Assumption B only involves linear independence. In practice, one wonders if it is important to position the targets so that the two sets of vectors are well conditioned? We will later show that the normal vectors are most important. In Fig. 2, we show an oriented tetrahedron⁴ where the normal vector of each face⁵ satisfies Assumption N and the orientation of the tetrahedron intersecting with the ring plane fulfills Assumption B.

Remark 3. The plane defined by the i -th target is $\mathcal{V}_i := \mathbf{p}_{0,i} + \mathbf{n}_i^\perp$. If we were to only use three targets, there would exist a unique point $\mathbf{q}_0 \in \mathbb{R}^3$ defined by

$$\mathbf{q}_0 := \bigcap_{i=1}^3 \mathcal{V}_i. \quad (5)$$

When (5) holds, the scale factor, s , is not unique; see Fig. 3. In other words, a ring plane passing through the point \mathbf{q}_0 leads to the scale factor s being unconstrained and therefore a unique answer does not exist. Therefore, it was critical to analyze target placement for the proposed method. A similar analysis seems to be missing for the baseline methods.

⁴Each of the four planar targets defines an infinite plane. The infinite planes create a tetrahedron.

⁵Faces of the tetrahedron are extended planes of the targets. Therefore, normal vectors of faces are normal vectors of targets.

IV. BASELINE INTRINSIC CALIBRATION METHODS

There are two standard calibration models for spinning LiDARs. They are based on spherical coordinates (ρ, θ, ϕ) , referred to as range, elevation and azimuth,

$$\begin{bmatrix} x \\ y \\ z \end{bmatrix} = f(\rho, \theta, \phi) = \begin{bmatrix} \rho \cos \theta \sin \phi \\ \rho \cos \theta \cos \phi \\ \rho \sin \theta \end{bmatrix}, \quad (6)$$

and the inverse function,

$$\begin{bmatrix} \rho \\ \theta \\ \phi \end{bmatrix} = f^{-1}(x, y, z) = \begin{bmatrix} \sqrt{x^2 + y^2 + z^2} \\ \sin^{-1}\left(\frac{z}{\sqrt{x^2 + y^2 + z^2}}\right) \\ \text{atan2}(x, y) \end{bmatrix}. \quad (7)$$

A. 3-Parameter Model

The most basic model [8] assumes the LiDAR measurements are made in spherical coordinates, (ρ, θ, ϕ) . Corrections to a measurement are given by a collection of offsets $\alpha := (\delta_\rho, \delta_\theta, \delta_\phi)$. Expressing the calibrated measurement in Cartesian coordinates gives

$$\Gamma_\alpha(\rho, \theta, \phi) := \begin{bmatrix} (\rho + \delta_\rho) \cos(\delta_\theta) \sin(\phi - \delta_\phi) \\ (\rho + \delta_\rho) \cos(\delta_\theta) \cos(\phi - \delta_\phi) \\ (\rho + \delta_\rho) \sin(\delta_\theta) \end{bmatrix} \quad (8)$$

Remark 4. (a) The nominal elevation for each ring is taken as zero; i.e., $\theta = 0$. (b) While it is not necessarily a drawback, most LiDAR interfaces only return a Cartesian representation of a measured point. For example, the ROS driver from Velodyne only provides the Cartesian coordinate and the intensity of a point. Hence, the user must assure the transformation to spherical coordinates, make the measurement correction coming from the calibration, and then transform back to Cartesian coordinates.

B. 6-Parameter Model

This model [9], [10] also works in spherical coordinates. In addition to the three offsets above, it includes s , a scale factor of ρ , h , a horizontal offset of the origin, and v , a vertical offset for the origin. The correction model becomes

$$\bar{\Gamma}_\alpha := \begin{bmatrix} (s\rho + \delta_\rho) \cos \delta_\theta \sin(\phi - \delta_\phi) - h \cos(\phi - \delta_\phi) \\ (s\rho + \delta_\rho) \cos \delta_\theta \cos(\phi - \delta_\phi) + h \sin(\phi - \delta_\phi) \\ (s\rho + \delta_\rho) \sin \delta_\theta + v \end{bmatrix}, \quad (9)$$

and therefore $\alpha := (\delta_\rho, \delta_\theta, \delta_\phi, s, h, v)$.

C. Can these transformations be expressed by elements of $\text{Sim}(3)$?

The short answer is no. When viewed in Cartesian coordinates, the calibration model (9) is fundamentally nonlinear and can be expressed as $\mathbf{R}_1(\mathbf{R}_2\mathbf{t}_1 + \mathbf{t}_2)$, where $\mathbf{R}_1, \mathbf{R}_2, \mathbf{t}_1$ and \mathbf{t}_2 depend on the measured point,

$$\mathbf{x}^\top = [x, y, z] \xrightarrow{f^{-1}} (\rho, \theta, \phi),$$

$$\mathbf{R}_1 = \begin{bmatrix} \sin(\phi - \delta_\phi) & -\cos(\phi - \delta_\phi) & 0 \\ \cos(\phi - \delta_\phi) & \sin(\phi - \delta_\phi) & 0 \\ 0 & 0 & 1 \end{bmatrix}, \quad (10)$$

$$\mathbf{R}_2\mathbf{t}_1 + \mathbf{t}_2 = \begin{bmatrix} \cos(\delta_\theta) & 0 & -\sin(\delta_\theta) \\ 0 & 1 & 0 \\ \sin(\delta_\theta) & 0 & \cos(\delta_\theta) \end{bmatrix} \begin{bmatrix} s\rho + \delta_\rho \\ 0 \\ 0 \end{bmatrix} + \begin{bmatrix} 0 \\ h \\ v \end{bmatrix}.$$

The calibration first applies a corrected elevation angle to a range value that has been offset and scaled. Next, the (y, z) position of the origin is offset, and lastly, a corrected rotation about the z -axis is applied.

D. Cost function for baseline models

For a given collection of points \mathcal{PC} , possibly from multiple targets $t \in \{1, \dots, T\}$, we seek calibration parameters that solve

$$\min_\alpha \sum_{t=1}^T \sum_{i=1}^{M_t} |\mathbf{n}_t^\top (F(\mathbf{x}_i, \alpha) - \mathbf{p}_{0,t})|, \quad (11)$$

where

- 1) for baseline model \mathbf{BL}_1 [8] in (8), $\alpha = (\delta_\rho, \delta_\theta, \delta_\phi)$ and

$$F(\mathbf{x}, \alpha) := \Gamma_\alpha \circ f^{-1}(\mathbf{x});$$

- 2) for baseline model \mathbf{BL}_2 [9], [10] in (9), $\alpha = (\delta_\rho, \delta_\theta, \delta_\phi, s, h, v)$ and

$$F(\mathbf{x}, \alpha) := \bar{\Gamma}_\alpha \circ f^{-1}(\mathbf{x}).$$

Remark 5. For the 3-parameter model \mathbf{BL}_1 , a single planar target is sufficient to uniquely determine a calibration. For the 6-parameter model \mathbf{BL}_2 , non-uniqueness can occur as outlined in Theorem 1 and Fig. 3.

V. GLOBAL OPTIMIZATION: FROM MIN TO MIN-MIN

Theorem 1 states that a unique answer exists. In this section, we propose a method to find it. In particular, we show a globally convergent algorithm to determine the element of the Lie Group that globally minimizes the cost function (2). This is done by converting the minimization problem in (3) to a Min-Min problem. The inner minimization problem has an efficient global solution by results in [17], [18]. The outer minimization is scalar, and it is easy to limit the range of interest to a compact set.

A. Problem Statement and Compact Sets

The intrinsic calibration problem is defined in (3):

$$\min_{s, \mathbf{R}, \mathbf{v}} J(s, \mathbf{R}, \mathbf{v}; \mathcal{X}_t, \mathbf{n}_t, \mathbf{p}_{0,t}), \quad (12)$$

where the cost is defined as

$$J(s, \mathbf{R}, \mathbf{v}) := \sum_{t=1}^T \sum_{i=1}^{M_t} |\mathbf{n}_t^\top (s\mathbf{R} \cdot \mathbf{x}_i + \mathbf{v} - \mathbf{p}_{0,t})|^2. \quad (13)$$

It is straightforward to show that J is a continuous function on $\text{Sim}(3)$. As a set, we write $\text{Sim}(3) = \mathbb{R}^+ \times \text{SO}(3) \times \mathbb{R}^3$, where $\mathbb{R}^+ := \mathbb{R} > 0$. Note that $\text{SO}(3)$ is compact. To guarantee that a minimum exists, we consider compact subsets of $s \in \mathbb{R}^+$ and $\mathbf{v} \in \mathbb{R}^3$ and define (12):

$$J^* := \min_{s, \mathbf{R}, \mathbf{v}} J(s, \mathbf{R}, \mathbf{v})$$

$$s^*, \mathbf{R}^*, \mathbf{v}^* := \arg \min_{s, \mathbf{R}, \mathbf{v}} J(s, \mathbf{R}, \mathbf{v}). \quad (14)$$

Algorithm 1: Proposed global optimizer

Input: Collections of points (\mathcal{X}_t) and corresponding targets ($\mathbf{n}_t, \mathbf{p}_{0,t}$)

Output: Global optimum $\mathbf{H}^* \in \text{Sim}(3)$

Initialization: Arbitrary initialization is allowable. We use $\mathbf{R} = \mathbf{I}, \mathbf{v} = \mathbf{0}$, and $s \in [0.8, 1.2]$

```

1 while  $k < \text{MAX\_ITER}$  do
2   // Scale the collections of points
    ${}^U_k \mathcal{X}_t^s \leftarrow {}^U_k s \cdot \mathcal{X}_t, {}^L_k \mathcal{X}_t^s \leftarrow {}^L_k s \cdot \mathcal{X}_t$ 
   // Compute the optimum  $\mathbf{R}, \mathbf{v}$  given the scaled points
3    ${}^L_k \mathbf{R} \leftarrow {}^L_k \mathcal{X}_t^s$  and (42) in [34],  ${}^L_k \mathbf{v} \leftarrow {}^L_k \mathbf{R}$  and (36) in [34]
4    ${}^U_k \mathbf{R} \leftarrow {}^U_k \mathcal{X}_t^s$  and (42) in [34],  ${}^U_k \mathbf{v} \leftarrow {}^U_k \mathbf{R}$  and (36) in [34]
   // Compute the P2P by current  $\mathbf{R}, \mathbf{v}$ 
5    ${}^L_k J \leftarrow (13)$  in [34],  ${}^U_k J \leftarrow (13)$  in [34]
   // Update  ${}^U_{k+1} s$  and  ${}^L_{k+1} s$ 
6    ${}^L_{k+1} s \leftarrow (21)$  in [34],  ${}^U_{k+1} s \leftarrow (21)$  in [34]
7 return  $s^*, \mathbf{R}^*, \mathbf{v}^*$ 

```

B. From Min to Min-Min

We use again the fact that $\text{Sim}(3) = \mathbb{R}^+ \times \text{SO}(3) \times \mathbb{R}^3$ to redefine (12) as a Min-Min problem.

Proposition 1.

$$\min_{s, \mathbf{R}, \mathbf{v}} J(s, \mathbf{R}, \mathbf{v}) = \min_s \min_{\mathbf{R}, \mathbf{v}} J(s, \mathbf{R}, \mathbf{v}), \quad (15)$$

where the minimums are taken over the same compact sets used in (14).

Proof: From (14), we have that

$$J^* = J(s^*, \mathbf{R}^*, \mathbf{v}^*). \quad (16)$$

We further introduce

$$\begin{aligned} h(s) &:= \min_{\mathbf{R}, \mathbf{v}} J(s, \mathbf{R}, \mathbf{v}) \\ h^* &:= \min_s h(s) \end{aligned} \quad (17)$$

and note that by definition, we have

$$J^* \leq h^*. \quad (18)$$

To show $h^* \leq J^*$, we use that minimizing values of J exist and hence

$$h^* \leq h(s^*) := \min_{\mathbf{R}, \mathbf{v}} J(s^*, \mathbf{R}, \mathbf{v}) \leq J(s^*, \mathbf{R}^*, \mathbf{v}^*) = J^*. \quad (19)$$

Equations (18) and (19) conclude the equivalency of (15). ■

From Proposition 1, we can define the intrinsic calibration problem as

$$f(s) := \min_{\mathbf{R}, \mathbf{v}} J(s, \mathbf{R}, \mathbf{v}; \mathcal{X}_t, \mathbf{n}_t, \mathbf{p}_{0,t}) \quad (20)$$

$$J^* = \min_s f(s). \quad (21)$$

C. Determining the Calibration Parameters

Because we can bound the scaling s to a compact set, a minimizing value can be found by dense search. In the Appendix C [34], we discuss a heuristic to speed up the algorithm if one feels the need.

At the $(k+1)$ -th iteration, the scaling parameter is determined and the remaining parameters correspond to $\text{SE}(3)$. To solve for them, we adopt techniques that were used to solve 3D registration or 3D SLAM [15]–[18] where the problem is formulated as a QCQP, and the Lagrangian dual relaxation is used. The relaxed problem becomes a Semidefinite Program (SDP) and convex. The problem can thus be solved globally and efficiently by off-the-shelf specialized solvers [19]. This process is summarized in Appendix B in [34]. As shown in [18], the dual relaxation is empirically always tight (the duality gap is zero). We also use the same simulation and experimental data set in [17], [18] to verify that the proposed algorithm is able to converge globally, see Appendix C in [34] for more visual results.

Remark 6. One may argue that the above is a standard optimization problem in that other solvers, such as *Google ceres* or *g2o*, can easily solve it. However, they are local solvers and will suffer if a good initial guess is not provided.

VI. SIMULATION AND EXPERIMENTAL RESULTS

This section first presents a simulation study of the intrinsic calibration problem that will show the importance of Theorem 1 for eliminating over parameterization of the proposed model. Results here will then be used to inform the experimental work. All experiments are conducted with a *32-Beam Velodyne ULTRA Puck LiDAR*, mounted on an in-house designed torso for a Cassie-series bipedal robot [35]. All the optimizations related to the proposed methods are solved via the proposed algorithm (see Algorithm 1). As for the two baselines, we implemented them and solved via the `fmincon` function in MATLAB. All the methods, simulator, solver, and datasets are open-sourced: [20]–[22].

A. Simulated LiDAR Environment

Due to lack of ground truth, we built a LiDAR simulator to compare our calibration method against the two baselines and to illustrate the role of target positioning. Our simulator can model LiDAR sensors of different working principles (spinning vs solid-state). With our simulator, it is easy to control sources of uncertainty, including both mechanical model uncertainty and measurement noise. Targets are assumed to be planar and polygonal.

To simulate 3D points on a planar target, we generate rays from the LiDAR sensor, and define a “target” point as the point at which the ray intersects the target. The simulator has an option to account for shadowing or not. After locating the exact LiDAR returns on the target, based on the LiDAR type, we then add two types of uncertainty to the returns and report them as measured data.

Remark 7. The simulator first finds all intersection points with the (infinite) plane defined by the target. To determine

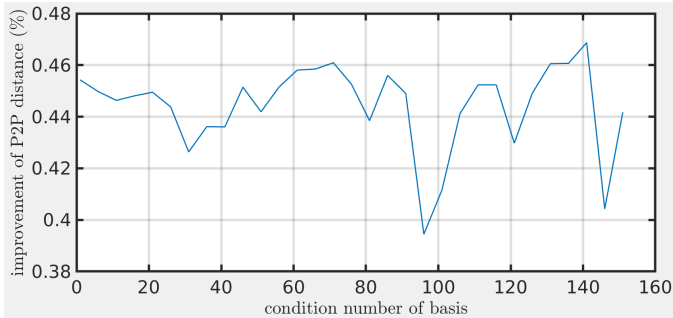


Fig. 4: P2P cost improvement is insensitive to condition number of the basis. The figure illustrates validation results for ten thousand orientations of four targets arranged as a tetrahedron. Each orientation is a calibration scene from which a set of calibration parameters is obtained. The calibration parameters are then applied to another complex scene for validation. This figure shows that regardless of the orientation of the tetrahedron, we are able to reduce the P2P cost by 44.7% on average.

if a point on the plane is within the boundary of the target polygon is a well-known problem in computer graphics, called the Point-In-Polygon (PIP) problem [36], [37]. The Winding Number algorithm [38] is implemented in this simulator. If the winding number of a point is not zero, the point lies inside the boundary; otherwise it is outside.

B. Intrinsic Calibration of Spinning LiDARs

1) *Illustration of Theorem 1 in simulation:* We randomly create 32 deterministic noise sequences (of length appropriate for each ring) and apply them to the ideal measurements of each ring in the LiDAR simulator. As a calibration scene, we arrange four targets around the LiDAR in the shape of a regular tetrahedron and then minimize the cost function in (3). For validation, we collect simulated data from a complex scene with 24 targets at various orientations and distances, using the same uncalibrated LiDAR corrupted by the same deterministic noise. We then applied the calibration parameters to the perturbed uncalibrated LiDAR measurements and reduced the P2P distance of the validation scene by 45.43% compared to the uncalibrated P2P distance. Additionally, to study the influence of different condition numbers in Assumption B on the calibration results, we rotate the tetrahedron with various orientations (ten thousand different orientations in total, yielding ten thousand different bases). We observe that the P2P cost improvement is insensitive to the condition number of the basis. In Fig. 4, the simulation results show that by using

the tetrahedron (regardless of the orientation) to calibrate the LiDAR, the P2P distance was reduced by 44.7% on average.

2) *Illustration of Theorem 1 in experiments:* Informed by the simulation study, two scenes (calibration and validation) of data from a 32-Beam Velodyne ULTRA Puck LiDAR were collected using the LiDARtag package [32], [39]. In Fig. 5, the calibration scene contains four targets⁶ arranged as an oriented tetrahedron as stated in Theorem 1. The targets' normal vectors are estimated using the L1-inspired method in [33].

In the raw data, the rings are mis-calibrated (by assumption). Because the target planes are estimated using data corresponding to mis-calibrated rings, the estimated normal vectors are inaccurate. We therefore propose a refinement of the normal vectors conditioned on the current estimate of the similarity transformation $\text{Sim}(3)$, that is, based on the current estimate of the intrinsic parameters $(s, \mathbf{R}, \mathbf{v})$. Once the normal vectors are updated, new estimates for $(s, \mathbf{R}, \mathbf{v})$ can be obtained, resulting in an alternating two-step process.

Figure 6 shows the experimental result of applying the calibration parameters to another set of targets (validation scene) placed at 0.7 meter. The proposed alternating method reduces the P2P distance by 68.6% with respect to the factory-calibrated LiDAR. Additionally, we induce varying levels of systematic errors (from 1 cm to 7 cm, corresponding to level 1 to level 7) to the experiment data to ensure the robustness of the proposed method, as shown in Table I. We observe that our proposed method is insensitive to systematic error. In addition, Table II shows the consistency of the proposed method as we accumulate different numbers of scans with different noise levels. It is seen that with higher levels of induced deterministic noise, the performance of the proposed method is invariant to the number of accumulated scans, while with lower levels of deterministic noise, the more scans included, the better is the performance. Both of these properties are desirable.

Remark 8. *There are two ways to orient the targets to form a tetrahedron: 1) put the targets around the LiDAR and keep the LiDAR pose fixed; 2) keep the target poses fixed and rotate the LiDAR. This will allow the targets to form a tetrahedron even if a LiDAR does not have a 360° field of view.*

⁶The targets were placed a distance of 0.7 meter so that most of the rings would lie on the targets.

TABLE I: Validation data for various calibration methods on a 32-Beam Velodyne ULTRA Puck LiDAR. The numbers are the average P2P distance in meters. For each column, the LiDAR's calibration parameters are optimized on a common set of four targets arranged as a tetrahedron and validated on a common set of three targets arranged in different orientations and at different distances. What varies in each column is the level of systematic noise added to the raw data, as reflected in the P2P error reported in the row for Factory Calibration. Noise 0 is the raw signal from the factory-calibrated LiDAR, while Noise 1 to Noise 7 have increasing levels of systematic error. Our proposed method is insensitive to systematic error.

	Methods	Noise 0	Noise 1	Noise 2	Noise 3	Noise 4	Noise 5	Noise 6	Noise 7
P2P	Factory Calibration	0.0140	0.0196	0.0309	0.0408	0.0486	0.0581	0.0669	0.0772
	Baseline1 (3 parameters)	0.0052	0.0054	0.0064	0.0085	0.0111	0.0135	0.0154	0.0164
	Baseline2 (6 parameters)	0.0042	0.0059	0.0070	0.0100	0.0121	0.0148	0.0165	0.0181
	Our Method	0.0047	0.0042	0.0040	0.0041	0.0043	0.0041	0.0039	0.0040
Point Clouds Thickness	Factory Calibration	0.0626	0.0777	0.1182	0.1579	0.1981	0.2379	0.2788	0.3211
	Baseline1 (3 parameters)	0.0439	0.0463	0.0634	0.0817	0.0998	0.1177	0.1347	0.1501
	Baseline2 (6 parameters)	0.0457	0.0535	0.0719	0.1005	0.1110	0.1308	0.1440	0.1694
	Our Method	0.0476	0.0475	0.0476	0.0582	0.0531	0.0464	0.0449	0.0450

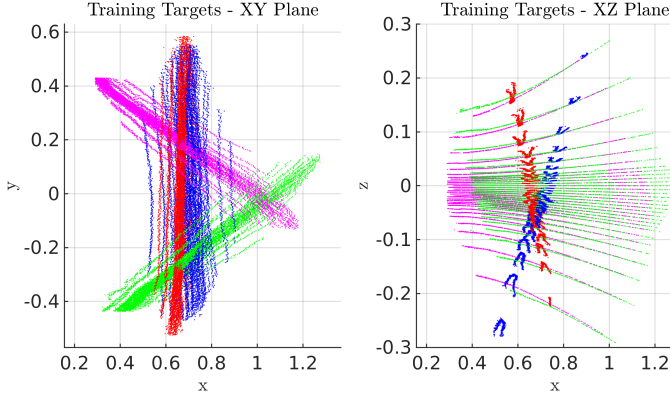


Fig. 5: Four targets are placed to form a tetrahedron. The left shows the top-down view (X - Y plane) of a single scan of the point cloud from the calibration scene and the right shows the side view (X - Z plane) of the scene. Different colors stand for different targets.

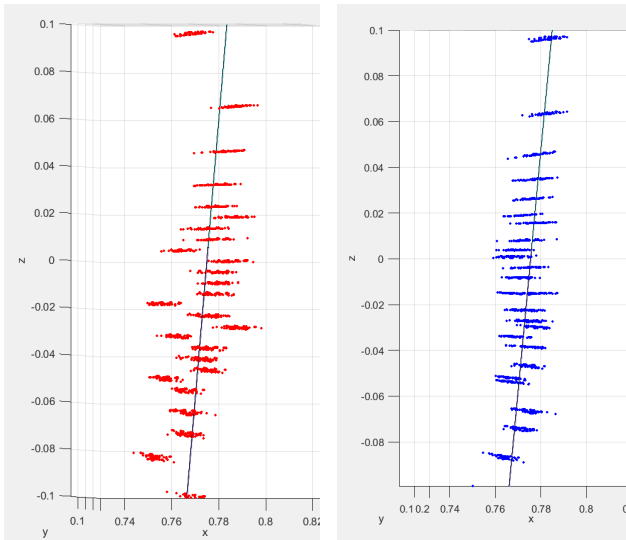


Fig. 6: On the left shows a factory-calibrated 32-Beam Velodyne ULTRA Puck LiDAR measuring on a planar target placed at 0.7 meter. The measurements are not consistent and lead to a thickness of 6.2 cm point cloud with 1.4 cm P2P distance. On the right shows the calibration results of the calibration parameters globally optimized over the tetrahedron calibration scene in Fig. 5 and then the parameters of each ring are applied to this dataset as validation. The thickness and P2P distance after calibration are 4.4 cm and 0.47 cm.

Remark 9. To decide if the P2P distance of a ring to a target is random noise or systematic errors, we first compute the standard deviation of the LiDAR returns on the target and consider the P2P distance greater than 3σ as systematic error.

C. LiDAR Simulated Intrinsic Calibration of Solid-State LiDARs

At the time of writing, we do not have access to a solid-state LiDAR; therefore only simulation results are provided. However, we are open to collaborating if the reader can share data. OPA solid-state LiDARs are fabricated on a planar wafer with a large number of emitters, see Sec. I. For such a LiDAR, we induce geometric uncertainty into a simulation of the system by assuming the plane of the wafer is slightly warped. In the simulator, the OPA solid-state LiDAR has 20×20 emitters with $160^\circ \times 40^\circ$ (horizontal, vertical) field of view. We place four targets of the same size in the simulator.

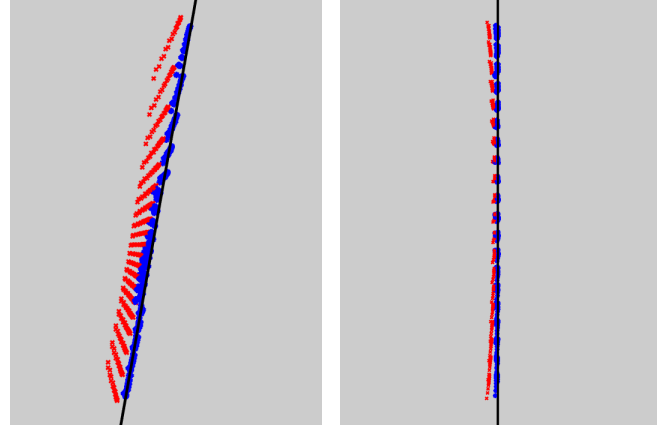


Fig. 7: A solid-state LiDAR is (hypothetically) built on a warped wafer and measures a planar target (black). The un-calibrated measurements and calibrated measurements are marked in red and blue, respectively. The left image shows a top-down view and the right image shows a side view of a target. The proposed method reduces the P2P distance by 48.7%.

Theorem 1 requires a ring plane, as mentioned in Sec. III-D. We therefore parse the LiDAR returns into 20×4 uniform grids over the planar targets, with each grid containing five points. Each grid plays the role of a ring plane in Theorem 1, resulting in a total of 80 calibration models. We use Weighted Least Squares to estimate the plane of the target. The calibrated sensor is then validated on four other scenes that have different angles and distances. The mean P2P cost of (3) improves by 48.7%; the result is visualized in Fig. 7.

Remark 10. The solid-state LiDAR is used to measure the same target four times with different orientations. The four target planes form a tetrahedron. Therefore, the same five points can scan the four planes and result in a ring plane. Instead of five points, we can group a row/column of points, as mentioned in Sec. III-B.

VII. CONCLUSIONS

We proposed a universal method for LiDAR intrinsic calibration that abstracts away the physics of a LiDAR type (spinning head vs. solid-state, for example) and focuses instead on the spatial geometry of the point cloud generated by the sensor. The calibration parameter becomes an element of $\text{Sim}(3)$, a matrix Lie group. We mathematically prove that given four targets with appropriate orientations, the proposed model is well-constrained (i.e., a unique answer exists). Because $\text{Sim}(3)$ is closely related to $\text{SE}(3)$, we showed how to profitably apply efficient, globally convergent algorithms for $\text{SE}(3)$ to determine a solution to our problem in $\text{Sim}(3)$. The resulting algorithm was evaluated in simulation for a solid-state LiDAR and simulation and experiment for a spinning LiDAR. The P2P distance of the validation scene for the spinning LiDAR was reduced 44.7% and 68.6% in simulation and experiment, respectively. The P2P distance of the validation scene for the solid-state LiDAR was reduced by 48.7%. Both simulation and experiments showed that the proposed method can serve as a generic model for intrinsic calibration of both spinning and solid-state LiDARs.

TABLE II: Consistency of the proposed methods. The numbers are the average P2P distance in meters and improvement of average P2P distance in percentage. The columns show the numbers of accumulated scans. It is seen that with higher levels of induced deterministic noise, the performance of the proposed method is invariant to the number of accumulated scans, while with lower levels of deterministic noise, the more scans included, the better is the performance. Both of these properties are desirable.

	Noise Level	1 scan	2 scans	4 scans	6 scans	8 scans	10 scans	12 scans
Original P2P	0	0.013998	0.013998	0.014616	0.014593	0.0144	0.01439	0.01439
Calibrated P2P		0.0047046	0.0047046	0.0040949	0.0040496	0.0040546	0.0040675	0.0040675
Improvement [%]		0.6639	0.6639	0.71983	0.7225	0.71844	0.71735	0.71735
Original P2P	2	0.030888	0.030861	0.029893	0.02983	0.029812	0.031767	0.031783
Calibrated P2P		0.0040332	0.0040739	0.0040189	0.0039899	0.0039737	0.0040665	0.0040417
Improvement [%]		0.86942	0.86799	0.86556	0.86625	0.86671	0.87199	0.87284
Original P2P	4	0.048608	0.047194	0.048691	0.050308	0.050269	0.050251	0.050254
Calibrated P2P		0.004301	0.0044295	0.004129	0.0040814	0.0040991	0.0040807	0.004067
Improvement [%]		0.91152	0.90614	0.9152	0.91887	0.91846	0.91879	0.91907
Original P2P	6	0.066834	0.066892	0.066869	0.06685	0.066823	0.066818	0.066838
Calibrated P2P		0.0043101	0.0044868	0.0044289	0.0044279	0.0044585	0.0044699	0.0044777
Improvement [%]		0.93551	0.93293	0.93377	0.93376	0.93328	0.9331	0.93301

ACKNOWLEDGMENT

Toyota Research Institute (TRI) provided funds to support this work. Funding for J. Grizzle was in part provided by TRI and in part by NSF Award No. 1808051. The first author thanks Wonhui Kim for useful conversations. The authors thank Carl Olsson for kindly providing the experimental datasets in [17].

REFERENCES

- [1] Z. Zhang, "A flexible new technique for camera calibration," *IEEE Trans. Pattern Anal. Mach. Intell.*, vol. 22, no. 11, pp. 1330–1334, 2000.
- [2] D. Liebowitz and A. Zisserman, "Metric rectification for perspective images of planes," in *Proc. IEEE Conf. Comput. Vis. Pattern Recog.* IEEE, 1998, pp. 482–488.
- [3] G. P. Stein, "Accurate internal camera calibration using rotation, with analysis of sources of error," in *Proc. IEEE Int. Conf. Comput. Vis.* IEEE, 1995, pp. 230–236.
- [4] J. Maye, P. Furgale, and R. Siegwart, "Self-supervised calibration for robotic systems," in *2013 IEEE Intelligent Vehicles Symposium (IV)*. IEEE, 2013, pp. 473–480.
- [5] Itseez, "Open source computer vision library," <https://github.com/itseez/opencv>, 2015.
- [6] M. Quigley, K. Conley, B. Gerkey, J. Faust, T. Foote, J. Leibs, R. Wheeler, and A. Y. Ng, "ROS: an open-source Robot Operating System," in *ICRA workshop on open source software*, 2009.
- [7] F. M. Mirzaei, D. G. Kottas, and S. I. Roumeliotis, "3D LiDAR–camera intrinsic and extrinsic calibration: Identifiability and analytical least-squares-based initialization," *Int. J. Robot. Res.*, vol. 31, no. 4, pp. 452–467, 2012.
- [8] G. Pandey, J. McBride, S. Savarese, and R. Eustice, "Extrinsic calibration of a 3D laser scanner and an omnidirectional camera," *IFAC Proceedings Volumes*, vol. 43, no. 16, pp. 336–341, 2010.
- [9] C. Glennie and D. D. Lichti, "Static calibration and analysis of the velodyne hdl-64e s2 for high accuracy mobile scanning," *Remote sensing*, vol. 2, no. 6, pp. 1610–1624, 2010.
- [10] H. Nouria, J.-E. Deschaud, and F. Goulette, "Point cloud refinement with a target-free intrinsic calibration of a mobile multi-beam LiDAR system," 2016.
- [11] T. Chan, D. D. Lichti, and D. Belton, "Temporal analysis and automatic calibration of the velodyne hdl-32e LiDAR system," *ISPRS Ann. Photogramm. Remote Sens. Spat. Inf. Sci.*, vol. 2, pp. 61–66, 2013.
- [12] G. Atanacio-Jiménez, J.-J. González-Barbosa, J. B. Hurtado-Ramos, F. J. Ornelas-Rodríguez, H. Jiménez-Hernández, T. García-Ramírez, and R. González-Barbosa, "LiDAR velodyne hdl-64e calibration using pattern planes," *International Journal of Advanced Robotic Systems*, vol. 8, no. 5, p. 59, 2011.
- [13] N. Muhammad and S. Lacroix, "Calibration of a rotating multi-beam LiDAR," in *Proc. IEEE/RSJ Int. Conf. Intell. Robots and Syst.* IEEE, 2010, pp. 5648–5653.
- [14] R. Bergelt, O. Khan, and W. Hardt, "Improving the intrinsic calibration of a velodyne LiDAR sensor," in *2017 IEEE SENSORS*. IEEE, 2017, pp. 1–3.
- [15] R. Tron, D. M. Rosen, and L. Carlone, "On the inclusion of determinant constraints in Lagrangian duality for 3D SLAM," in *Robotics: Science and Systems (RSS) in the workshop "The Problem of Mobile Sensors*, 2015.
- [16] L. Carlone, D. M. Rosen, G. Calafiore, J. J. Leonard, and F. Dellaert, "Lagrangian duality in 3D SLAM: Verification techniques and optimal solutions," in *2015 IEEE/RSJ International Conference on Intelligent Robots and Systems (IROS)*. IEEE, 2015, pp. 125–132.
- [17] C. Olsson and A. Eriksson, "Solving quadratically constrained geometrical problems using Lagrangian duality," in *2008 19th International Conference on Pattern Recognition*. IEEE, 2008, pp. 1–5.
- [18] J. Briaies and J. Gonzalez-Jimenez, "Convex global 3D registration with Lagrangian duality," in *Proceedings of the IEEE Conference on Computer Vision and Pattern Recognition*, 2017, pp. 4960–4969.
- [19] M. Grant and S. Boyd, "CVX: Matlab software for disciplined convex programming, version 2.1," 2014.
- [20] J.K. Huang, C. Feng, M. Achar, M. Ghaffari and Jessy W. Grizzle, "Intrinsic LiDAR Calibration," 2019. [Online]. Available: https://github.com/UMich-BipedLab/LiDAR_intrinsic_calibration
- [21] J.K. Huang, C. Feng and Jessy W. Grizzle, "LiDAR Simulator Package," 2020. [Online]. Available: https://github.com/UMich-BipedLab/lidar_simulator
- [22] J.K. Huang, C. Feng, M. Achar, M. Ghaffari and Jessy W. Grizzle, "Global Sim3 Solver," 2020. [Online]. Available: https://github.com/UMich-BipedLab/global_sim3_solver
- [23] A. Frederiksen and S. Hartmann, "LiDAR device including at least one diffuser element," Feb. 6 2020, uS Patent App. 16/525,010.
- [24] C. V. Poulton, M. J. Byrd, P. Russo, E. Timurdogan, M. Khandaker, D. Vermeulen, and M. R. Watts, "Long-range LiDAR and free-space data communication with high-performance optical phased arrays," *IEEE Journal of Selected Topics in Quantum Electronics*, vol. 25, no. 5, pp. 1–8, 2019.
- [25] C. V. Poulton, P. Russo, E. Timurdogan, M. Whitson, M. J. Byrd, E. Hosseini, B. Moss, Z. Su, D. Vermeulen, and M. R. Watts, "High-performance integrated optical phased arrays for chip-scale beam steering and LiDAR," in *CLEO: Applications and Technology*. Optical Society of America, 2018, pp. ATu3R–2.
- [26] H. W. Yoo, N. Druml, D. Brunner, C. Schwarzl, T. Thurner, M. Hennecke, and G. Schitter, "Mems-based LiDAR for autonomous driving," *e & i Elektrotechnik und Informationstechnik*, vol. 135, no. 6, pp. 408–415, 2018.
- [27] G. Pelz and N. Elbel, "Matrix light source and detector device for solid-state LiDAR," Feb. 6 2020, uS Patent App. 16/052,862.
- [28] N. Druml, I. Maksymova, T. Thurner, D. van Lierop, M. Hennecke, and A. Foroutan, "1d mems micro-scanning LiDAR," in *Conference on Sensor Device Technologies and Applications (SENSORDEVICES)*, vol. 9, 2018.
- [29] X. Lee and C. Wang, "Optical design for uniform scanning in mems-based 3D imaging LiDAR," *Applied optics*, vol. 54, no. 9, pp. 2219–2223, 2015.

- [30] D. Wang, C. Watkins, and H. Xie, "Mems mirrors for LiDAR: A review," *Micromachines*, vol. 11, no. 5, p. 456, 2020.
- [31] P. García-Gómez, S. Royo, N. Rodrigo, and J. R. Casas, "Geometric model and calibration method for a solid-state LiDAR," *Sensors*, vol. 20, no. 10, p. 2898, 2020.
- [32] Jiunn-Kai Huang, Shoutian Wang, Maani Ghaffari, and Jessie W. Grizzle, "LiDARtag: A Real-Time Fiducial Tag System for Point Clouds," *arXiv preprint arXiv:1908.10349*, 2020.
- [33] J. Huang and J. W. Grizzle, "Improvements to target-based 3d lidar to camera calibration," *IEEE Access*, vol. 8, pp. 134 101–134 110, 2020.
- [34] J.-K. Huang, C. Feng, M. Achar, M. Ghaffari, and J. W. Grizzle, "Global unifying intrinsic calibration for spinning and solid-state lidars," *arXiv preprint arXiv:2012.03321*, 2020.
- [35] J. Huang. (2019) Cassie Blue walks Around the Wavefield. <https://youtu.be/LhFC45jweFMc>.
- [36] M. M. Moscato, L. Titolo, M. A. Feliú, and C. A. Muñoz, "Provably correct floating-point implementation of a point-in-polygon algorithm," in *International Symposium on Formal Methods*. Springer, 2019, pp. 21–37.
- [37] M. El-Salamony and A. Guaily, "Enhanced modified-polygon method for point-in-polygon problem," in *Recent Advances in Engineering Mathematics and Physics*. Springer, 2020, pp. 47–61.
- [38] D. Alciatore and R. Miranda, "A winding number and point-in-polygon algorithm," *Glaxo Virtual Anatomy Project Research Report, Department of Mechanical Engineering, Colorado State University*, 1995.
- [39] Jiunn-Kai Huang, Shoutian Wang, Maani Ghaffari, and Jessie W. Grizzle, "LiDARtag ROS Package," 2020. [Online]. Available: <https://github.com/UMich-BipedLab/LiDARtag>
- [40] J. Brewer, "Kronecker products and matrix calculus in system theory," *IEEE Transactions on circuits and systems*, vol. 25, no. 9, pp. 772–781, 1978.
- [41] Paul L. Fackler, "Notes on Matrix Calculus," 2005. [Online]. Available: <https://media.gradebuddy.com/documents/1897145/1ad5e235-824d-4bbf-81d6-ffd2040e37ec.pdf>

APPENDIX A
PROOF ON UNIQUENESS OF SIMILARITY
TRANSFORMATION

The proof provides a guideline to place targets such that an answer to the optimization problem is unique. In particular, under Assumption N and Assumption B, the optimization problem has only one unique answer. As stated in Sec. III, the intrinsic calibration parameters are modeled as an element of the similarity Lie group ($\text{Sim}(3)$). An element of this group in matrix form is

$$\mathbf{H} = \begin{bmatrix} s\mathbf{R} & \mathbf{t} \\ \mathbf{0} & 1 \end{bmatrix} \in \text{Sim}(3), \quad (22)$$

where $\mathbf{R} \in \text{SO}(3)$, $\mathbf{t} \in \mathbb{R}^3$ and $s \in \mathbb{R}^+$.

A. Mathematical Definitions and Preliminaries

Let $[S]$ and $[S]^\perp$ be the span and its orthogonal complement of $S \subset \mathbb{R}^3$, respectively⁷. We denote the union of intersection of K spans as $([S_1] + [S_2] + \dots + [S_K]) = \cap_{i=1}^K [S_i]$. Let $\mathbf{P} \subset \mathbb{R}^3$ be a plane. \mathbf{P} modeled the set traced out by a single ring of a perfectly calibrated spinning LiDAR. Let $\{\mathbf{e}_1, \mathbf{e}_2, \mathbf{e}_3\}$ denote the canonical basis for \mathbb{R}^3 . Without loss of generality, we assume $\mathbf{P} = [\mathbf{e}_3]^\perp = \{\mathbf{e}_1, \mathbf{e}_2\}$. Therefore, $\forall s > 0, \mathbf{R} \in \text{SO}(3)$,

$$(s\mathbf{R} - \mathbf{I})(\mathbf{P}) = 0 \iff s = 1, \mathbf{R} = \mathbf{I}^8$$

B. Assumptions

Consider four targets with unit normal vectors \mathbf{n}_i and let $\mathbf{p}_{0,i}$ be a points on the i -th target.

Assumption N (Normal Vectors)

All sets of three distinct vectors from $\{\mathbf{n}_1, \mathbf{n}_2, \mathbf{n}_3, \mathbf{n}_4, \mathbf{e}_3\}$ are linearly independent.

For $1 \leq i \leq 4$, the plane defined by the i -th target is $\mathbf{V}_i := \mathbf{p}_{0,i} + [\mathbf{n}_i]^\perp$. Under Assumption N, some facts are listed below without proofs:

- (a) For each $i \neq j \in \{1, 2, 3, 4\}$, $\mathbf{p}_{ij} := \mathbf{P} \cap \mathbf{V}_i \cap \mathbf{V}_j$ exists and is unique. There are $\binom{4}{2}$ intersection points.
- (b) $\mathbf{V}_i \cap \mathbf{V}_j = \mathbf{p}_{ij} + [\mathbf{n}_i, \mathbf{n}_j]^\perp$.
- (c) $\mathbf{H} \cdot \mathbf{p}_{ij} \in \mathbf{V}_i \cap \mathbf{V}_j$ if, and only if,

$$(s\mathbf{R} - \mathbf{I})\mathbf{p}_{ij} + \mathbf{t} \in [\mathbf{n}_i, \mathbf{n}_j]^\perp.$$

- (d) Because $\dim[\mathbf{n}_i, \mathbf{n}_j]^\perp = 1$, $(s\mathbf{R} - \mathbf{I})\mathbf{p}_{ij} + \mathbf{t} \neq 0$ if, and only if, $[(s\mathbf{R} - \mathbf{I})\mathbf{p}_{ij} + \mathbf{t}] = [\mathbf{n}_i, \mathbf{n}_j]^\perp$.
- (e) Let $\{\mathbf{p}_a, \mathbf{p}_b\}$ be a basis for \mathbf{P} . Then $(s\mathbf{R} - \mathbf{I})(\mathbf{P}) = 0$ if, and only if, $(s\mathbf{R} - \mathbf{I})(\mathbf{p}_a) = 0$ and $(s\mathbf{R} - \mathbf{I})(\mathbf{p}_b) = 0$.

Assumption B (Basis Vectors)

Given the six intersection points, any two form a set of basis for the ring plane. There are $\binom{6}{2}$ sets of basis. Subsets of the basis' are linearly independent.

- (a) $\{\mathbf{p}_{12}, \mathbf{p}_{13}\}, \{\mathbf{p}_{13}, \mathbf{p}_{14}\}, \{\mathbf{p}_{14}, \mathbf{p}_{12}\}$,
- (b) $\{\mathbf{p}_{12}, \mathbf{p}_{23}\}, \{\mathbf{p}_{23}, \mathbf{p}_{24}\}, \{\mathbf{p}_{24}, \mathbf{p}_{12}\}$,
- (c) $\{\mathbf{p}_{13}, \mathbf{p}_{23}\}, \{\mathbf{p}_{23}, \mathbf{p}_{34}\}, \{\mathbf{p}_{34}, \mathbf{p}_{13}\}$,
- (d) $\{\mathbf{p}_{14}, \mathbf{p}_{24}\}, \{\mathbf{p}_{24}, \mathbf{p}_{34}\}, \{\mathbf{p}_{34}, \mathbf{p}_{14}\}$,
- (e) $\{\mathbf{p}_{14}, \mathbf{p}_{23}\}$

C. A Complete Proof

Theorem 1. Assume that Assumptions N and B hold and let $\mathbf{H} \in \text{Sim}(3)$. If for each $i \neq j \in \{1, 2, 3, 4\}$, $\mathbf{H} \cdot \mathbf{p}_{ij} \in \mathbf{V}_i \cap \mathbf{V}_j$, then

$$\mathbf{H} = \begin{bmatrix} \mathbf{I} & \mathbf{0} \\ \mathbf{0} & 1 \end{bmatrix}. \quad (23)$$

Proof. The proof is by exhaustion on the dimension of $(s\mathbf{R} - \mathbf{I})(\mathbf{P})$. We have that $\mathbf{H} \cdot \mathbf{p}_{ij} = s\mathbf{R}\mathbf{p}_{ij} + \mathbf{t}$, and therefore

$$\mathbf{H} \cdot \mathbf{p}_{ij} \in \mathbf{V}_i \cap \mathbf{V}_j \iff (s\mathbf{R} - \mathbf{I})\mathbf{p}_{ij} + \mathbf{t} \in [\mathbf{n}_i, \mathbf{n}_j]^\perp. \quad (24)$$

- **Case 1:** $\dim(s\mathbf{R} - \mathbf{I})(\mathbf{P}) = 0$.

Then $\mathbf{t} \in [\mathbf{n}_i, \mathbf{n}_j]^\perp$ for all $i \neq j$. Hence, $\mathbf{t} \in [\mathbf{n}_1, \mathbf{n}_2]^\perp \cap [\mathbf{n}_2, \mathbf{n}_3]^\perp = 0$, which implies that $\mathbf{t} = 0$. Therefore, by **Simple Fact 1**, we are done. We next show that $\dim(s\mathbf{R} - \mathbf{I})(\mathbf{P}) > 0$ and $\mathbf{H} \cdot \mathbf{p}_{ij} \in \mathbf{V}_i \cap \mathbf{V}_j$ for all $i \neq j$ lead to contradictions.

- **Case 2:** $\dim(s\mathbf{R} - \mathbf{I})(\mathbf{P}) = 1$

(a) Suppose $\mathbf{t} \notin (s\mathbf{R} - \mathbf{I})(\mathbf{P})$. Then, for any \mathbf{p}_{ij} , $(s\mathbf{R} - \mathbf{I})\mathbf{p}_{ij} + \mathbf{t} \neq 0$. Hence,

$$\begin{aligned} [\mathbf{n}_1, \mathbf{n}_2]^\perp &= [(s\mathbf{R} - \mathbf{I})(\mathbf{p}_{12}) + \mathbf{t}] \\ [\mathbf{n}_2, \mathbf{n}_3]^\perp &= [(s\mathbf{R} - \mathbf{I})(\mathbf{p}_{23}) + \mathbf{t}] \\ [\mathbf{n}_3, \mathbf{n}_4]^\perp &= [(s\mathbf{R} - \mathbf{I})(\mathbf{p}_{34}) + \mathbf{t}]. \end{aligned}$$

Because $[\mathbf{n}_1, \mathbf{n}_2] \cap [\mathbf{n}_2, \mathbf{n}_3] \cap [\mathbf{n}_3, \mathbf{n}_4] = 0$, we have that $[\mathbf{n}_1, \mathbf{n}_2]^\perp + [\mathbf{n}_2, \mathbf{n}_3]^\perp + [\mathbf{n}_3, \mathbf{n}_4]^\perp = \mathbb{R}^3$. We deduce that $\dim(s\mathbf{R} - \mathbf{I})(\mathbf{P}) = 2$, which is a contradiction.

(b) Suppose $\mathbf{t} \in (s\mathbf{R} - \mathbf{I})(\mathbf{P})$ and thus there exists $\mathbf{p}_t \in \mathbf{P}$ such that $\mathbf{t} = (s\mathbf{R} - \mathbf{I})(\mathbf{p}_t)$. The condition (24) can therefore be written as

$$\mathbf{H} \cdot \mathbf{p}_{ij} \in \mathbf{V}_i \cap \mathbf{V}_j \iff (s\mathbf{R} - \mathbf{I})(\mathbf{p}_{ij} + \mathbf{p}_t) \perp \{\mathbf{n}_i, \mathbf{n}_j\}. \quad (25)$$

Because $\{\mathbf{p}_{12}, \mathbf{p}_{13}\}, \{\mathbf{p}_{13}, \mathbf{p}_{14}\}, \{\mathbf{p}_{14}, \mathbf{p}_{12}\}$ are bases for \mathbf{P} , we conclude that

$$[\mathbf{p}_{12} + \mathbf{p}_t, \mathbf{p}_{13} + \mathbf{p}_t, \mathbf{p}_{14} + \mathbf{p}_t] = \mathbf{P}. \quad (26)$$

Applying (25) to this set of vectors, we deduce that

$$(s\mathbf{R} - \mathbf{I})(\mathbf{P}) \perp \mathbf{n}_1.$$

Applying the same reasoning to $\{\mathbf{p}_{12}, \mathbf{p}_{23}\}, \{\mathbf{p}_{23}, \mathbf{p}_{24}\}, \{\mathbf{p}_{24}, \mathbf{p}_{12}\}$, we deduce that $(s\mathbf{R} - \mathbf{I})(\mathbf{P}) \perp \mathbf{n}_2$. Repeating again, we have $(s\mathbf{R} - \mathbf{I})(\mathbf{P}) \perp \mathbf{n}_3$ and thus $\dim(s\mathbf{R} - \mathbf{I})(\mathbf{P}) = 0$.

- **Case 3:** $\dim(s\mathbf{R} - \mathbf{I})(\mathbf{P}) = 2$

⁷. $S \subset \mathbb{R}^3, [S] = \mathbb{R}^3 \iff [S]^\perp = 0$

⁸ $(s\mathbf{R} - \mathbf{I})(\mathbf{P}) = [(s\mathbf{R} - \mathbf{I})\mathbf{e}_1] + [(s\mathbf{R} - \mathbf{I})\mathbf{e}_2]$

We rewrite (24) as

$$\mathbf{H} \cdot \mathbf{p}_{ij} \in \mathbf{V}_i \cap \mathbf{V}_j \iff -\mathbf{t} \in (\mathbf{sR} - \mathbf{I})\mathbf{p}_{ij} + [\mathbf{n}_i, \mathbf{n}_j]^\perp. \quad (27)$$

Hence, if for all $i \neq j \in \{1, 2, 3, 4\}$, $\mathbf{H} \cdot \mathbf{p}_{ij} \in \mathbf{V}_i \cap \mathbf{V}_j$, then the lines $(\mathbf{sR} - \mathbf{I})\mathbf{p}_{ij} + [\mathbf{n}_i, \mathbf{n}_j]^\perp$ in \mathbb{R}^3 must have a common point of intersection, namely $-\mathbf{t}$ and hence

$$\bigcap_{i \neq j \in \{1, 2, 3, 4\}} \{(\mathbf{sR} - \mathbf{I})\mathbf{p}_{ij} + [\mathbf{n}_i, \mathbf{n}_j]^\perp\} \neq \emptyset. \quad (28)$$

Remark 11. When $(\mathbf{sR} - \mathbf{I})(\mathbf{P}) = 0$, the intersections in (28) are non-empty; indeed, the equation reduces to

$$\bigcap_{i \neq j \in \{1, 2, 3, 4\}} [\mathbf{n}_i, \mathbf{n}_j]^\perp = \left(\sum_{i \neq j} [\mathbf{n}_i, \mathbf{n}_j] \right)^\perp = (\mathbb{R}^3)^\perp = 0,$$

and hence $\mathbf{t} = 0$.

In the remainder of the proof, we show the intersection being non-empty contradicts $\dim(\mathbf{sR} - \mathbf{I})(\mathbf{P}) = 2$. We do this by examining the intersections in (28) pairwise to arrive at a set of necessary conditions for $\mathbf{H} \cdot \mathbf{p}_{ij} \in \mathbf{V}_i \cap \mathbf{V}_j$ for $i \neq j$, and then use the necessary conditions to complete the proof. We note that for $ij \neq kl$,

$$\begin{aligned} & \{(\mathbf{sR} - \mathbf{I})\mathbf{p}_{ij} + [\mathbf{n}_i, \mathbf{n}_j]^\perp\} \cap \{(\mathbf{sR} - \mathbf{I})\mathbf{p}_{kl} + [\mathbf{n}_k, \mathbf{n}_l]^\perp\} \neq \emptyset \\ & \iff (\mathbf{sR} - \mathbf{I})(\mathbf{p}_{ij} - \mathbf{p}_{kl}) \in [\mathbf{n}_i, \mathbf{n}_j]^\perp + [\mathbf{n}_k, \mathbf{n}_l]^\perp. \end{aligned}$$

The indices are a bit easier to keep track of if we set

$$\begin{aligned} \mathbf{q}_1 &:= (\mathbf{sR} - \mathbf{I})(\mathbf{p}_{12}), \quad \mathbf{U}_1 := [\mathbf{n}_1, \mathbf{n}_2]^\perp \\ \mathbf{q}_2 &:= (\mathbf{sR} - \mathbf{I})(\mathbf{p}_{13}), \quad \mathbf{U}_2 := [\mathbf{n}_1, \mathbf{n}_3]^\perp \\ \mathbf{q}_3 &:= (\mathbf{sR} - \mathbf{I})(\mathbf{p}_{23}), \quad \mathbf{U}_3 := [\mathbf{n}_1, \mathbf{n}_4]^\perp \\ \mathbf{q}_4 &:= (\mathbf{sR} - \mathbf{I})(\mathbf{p}_{14}), \quad \mathbf{U}_4 := [\mathbf{n}_2, \mathbf{n}_3]^\perp, \end{aligned}$$

where $\{\mathbf{U}_k | k = 1, \dots, 4\}$ denote the indicated one-dimensional subspaces. Then, for each $i \neq j \in \{1, 2, 3, 4\}$, $\mathbf{U}_i \cap \mathbf{U}_j = 0$, and we have $\mathbf{U}_1 \oplus \mathbf{U}_2 \oplus \mathbf{U}_3 = \mathbb{R}^3$. Let \mathbf{u}_i be a basis for \mathbf{U}_i , so that $\mathbf{U}_i = [\mathbf{u}_i]$, and write

$$\mathbf{u}_4 = \alpha \mathbf{u}_1 + \beta \mathbf{u}_2 + \gamma \mathbf{u}_3.$$

Claim 1

Each of the coefficients α, β, γ is non-zero.

Proof. Suppose $\alpha = 0$. Then $\mathbf{U}_4 \subset \mathbf{U}_2 + \mathbf{U}_3$, that is,

$$[\mathbf{n}_2, \mathbf{n}_3]^\perp \subset [\mathbf{n}_1, \mathbf{n}_3]^\perp + [\mathbf{n}_1, \mathbf{n}_4]^\perp$$

But this is equivalent to

$$[\mathbf{n}_1] = [\mathbf{n}_1, \mathbf{n}_3] \cap [\mathbf{n}_1, \mathbf{n}_4] \subset [\mathbf{n}_2, \mathbf{n}_3],$$

and hence $\{\mathbf{n}_1, \mathbf{n}_2, \mathbf{n}_3\}$ is not linearly independent, contradicting Assumption N. The same argument holds for the other coefficients. ■

Claim 2

A necessary condition for

$$\bigcap_{i=1}^4 \{\mathbf{q}_i + \mathbf{U}_i\} \neq \emptyset \quad (29)$$

is that there exist real numbers c_1, c_2, c_3, c_4 such that

$$\begin{aligned} \Delta \mathbf{q}_{12} &:= \mathbf{q}_1 - \mathbf{q}_2 = c_1 \mathbf{u}_1 + c_2 \mathbf{u}_2 \\ \Delta \mathbf{q}_{13} &:= \mathbf{q}_1 - \mathbf{q}_3 = c_1 \mathbf{u}_1 + c_3 \mathbf{u}_3 \\ \Delta \mathbf{q}_{14} &:= \mathbf{q}_1 - \mathbf{q}_4 = c_1 \mathbf{u}_1 + c_4 \mathbf{u}_4 \\ \Delta \mathbf{q}_{23} &:= \mathbf{q}_2 - \mathbf{q}_3 = c_3 \mathbf{u}_3 - c_2 \mathbf{u}_2 \\ \Delta \mathbf{q}_{24} &:= \mathbf{q}_2 - \mathbf{q}_4 = c_4 \mathbf{u}_4 - c_2 \mathbf{u}_2 \\ \Delta \mathbf{q}_{34} &:= \mathbf{q}_3 - \mathbf{q}_4 = c_3 \mathbf{u}_3 - c_4 \mathbf{u}_4 \end{aligned} \quad (30)$$

Proof. Each row of (30) corresponds to a condition of the form $\mathbf{q}_i - \mathbf{q}_j \in \mathbf{U}_i \oplus \mathbf{U}_j$. The proof proceeds by expressing each of the six rows in (30) with distinct coefficients (12 in total), and then writing down three necessary compatibility conditions,

$$\begin{aligned} \Delta \mathbf{q}_{12} - \Delta \mathbf{q}_{13} + \Delta \mathbf{q}_{23} &= 0 \\ \Delta \mathbf{q}_{12} - \Delta \mathbf{q}_{14} + \Delta \mathbf{q}_{24} &= 0 \\ \Delta \mathbf{q}_{14} - \Delta \mathbf{q}_{13} + \Delta \mathbf{q}_{34} &= 0. \end{aligned} \quad (31)$$

Because $-\mathbf{t}$ is in the intersection of the lines in (29), the resulting linear equations must have a solution, and indeed direct computation shows that the set of solutions can be parameterized as given in the claim. ■

The next step is to note that $[\Delta \mathbf{q}_{12}, \dots, \Delta \mathbf{q}_{34}] \subset (\mathbf{sR} - \mathbf{I})(\mathbf{P})$, and hence its dimension must be less than three. Additional straightforward calculations show that

$$\dim [\Delta \mathbf{q}_{12}, \Delta \mathbf{q}_{13}, \Delta \mathbf{q}_{34}] = \text{rank} \begin{bmatrix} c_1 & c_1 & -\alpha c_4 \\ c_2 & 0 & c_2 - \beta c_4 \\ 0 & c_3 & -\gamma c_4 \end{bmatrix}.$$

In light of Claim 1, the rank is less than three if, and only if, any two coefficients of $\{c_1, c_2, c_3, c_4\}$ are zero. But if this is the case, then at least one row of (30) must be zero. Each row of (30), however, has the form $(\mathbf{sR} - \mathbf{I})(\mathbf{p}_a - \mathbf{p}_b)$, where $\{\mathbf{p}_a, \mathbf{p}_b\}$ is a basis for \mathbf{P} , and thus it cannot be the case that $\dim(\mathbf{sR} - \mathbf{I})(\mathbf{P}) = 2$. This completes the proof. ■

APPENDIX B
LAGRANGIAN DUALITY RELAXATION
FOR P2P DISTANCE ON SE(3)

At the k -th iteration, the scaling parameter is determined (see Sec. V) and the rest of the parameters are SE(3). To solve the remaining parameters, we adopt techniques that were used to solve 3D registration or 3D SLAM [15]–[18]. We summarize below for completeness. The action of SE(3) on \mathbb{R}^3 can be rewritten as:

$$\mathbf{H} \cdot \mathbf{x} = \mathbf{R}\mathbf{x} + \mathbf{v} = \begin{bmatrix} \mathbf{x}^\top \otimes I_3 & I_3 \end{bmatrix} \underbrace{\begin{bmatrix} \text{vec}(\mathbf{R}) \\ \mathbf{v} \end{bmatrix}}_{\boldsymbol{\tau}}, \quad (32)$$

where \otimes and $\text{vec}(\cdot)$ are the Kronecker product [40] and the vectorization operation [41], respectively.

A. P2P Distance Reformulation and Quadratic Formulation

The P2P distance (2) can be equivalently reformulated into a quadratic form:

$$\begin{aligned} \sum_{i=1}^M J_i &:= \sum_{i=1}^M |(\mathbf{H} \cdot \mathbf{x}_i - \mathbf{p}_{0,t})^\top (\mathbf{n}_t \mathbf{n}_t^\top) (\mathbf{H} \cdot \mathbf{x}_i \mathbf{p}_{0,t})| \\ &= \sum_{i=1}^M \begin{bmatrix} \tau \\ 1 \end{bmatrix}^\top N_i^\top (\mathbf{n}_t \mathbf{n}_t^\top) N_i \begin{bmatrix} \tau \\ 1 \end{bmatrix} = \tilde{\boldsymbol{\tau}}^\top W_t \tilde{\boldsymbol{\tau}}, \end{aligned} \quad (33)$$

where $N_i = [\mathbf{x}_i \otimes I_3 | -\mathbf{p}_{0,t}]$ and $W_t = \sum_i^M N_i^\top (\mathbf{n}_t \mathbf{n}_t^\top) N_i$. After rearranging (33), the resulting problem in (3) becomes

$$\begin{aligned} &\min_{H \in \text{SE}(3)} \sum_{t=1}^T \begin{bmatrix} \text{vec}(\mathbf{R}) \\ 1 \\ \mathbf{v} \end{bmatrix}^\top \tilde{W}'_t \begin{bmatrix} \text{vec}(\mathbf{R}) \\ 1 \\ \mathbf{v} \end{bmatrix} \\ &= \min_{H \in \text{SE}(3)} \sum_{t=1}^T \begin{bmatrix} \tilde{\mathbf{r}} \\ \mathbf{v} \end{bmatrix}^\top \begin{bmatrix} \tilde{W}_{\tilde{\mathbf{r}}, \tilde{\mathbf{r}}} & \tilde{W}_{\tilde{\mathbf{r}}, \mathbf{v}} \\ \tilde{W}_{\mathbf{v}, \tilde{\mathbf{r}}} & W_{\mathbf{v}, \mathbf{v}} \end{bmatrix}_t \begin{bmatrix} \tilde{\mathbf{r}} \\ \mathbf{v} \end{bmatrix} \\ &= \min_{H \in \text{SE}(3)} \tilde{\mathbf{r}}^\top \tilde{W}_{\tilde{\mathbf{r}}, \tilde{\mathbf{r}}} \tilde{\mathbf{r}} + 2\mathbf{v}^\top \tilde{W}_{\mathbf{v}, \tilde{\mathbf{r}}} \tilde{\mathbf{r}} + \mathbf{v}^\top W_{\mathbf{v}, \mathbf{v}} \mathbf{v} \end{aligned} \quad (34)$$

where $\tilde{\mathbf{r}} = [\text{vec}(\mathbf{R})^\top \ 1]^\top$. We then introduce the Lagrangian multipliers. Due to $R \in \text{SO}(3)$ constraints, the derivative with

respect to \mathbf{v} is zero: $\partial L(H, \lambda) / \partial \mathbf{v} = 0$, which leads to

$$\mathbf{v}^* = -(W_{\mathbf{v}, \mathbf{v}})^{-1} \tilde{W}_{\mathbf{v}, \tilde{\mathbf{r}}} \tilde{\mathbf{r}}. \quad (35)$$

By substituting (35) into (34), we have

$$\min_{\mathbf{R} \in \text{SO}(3)} \tilde{\mathbf{r}}^\top \tilde{\mathbf{Q}} \tilde{\mathbf{r}}, \quad (36)$$

where $\tilde{\mathbf{Q}}$ is the Schur complement of \tilde{W}'_t and equal to $\tilde{W}_{\tilde{\mathbf{r}}, \tilde{\mathbf{r}}} - \tilde{W}_{\tilde{\mathbf{r}}, \mathbf{v}} W_{\mathbf{v}, \mathbf{v}}^{-1} \tilde{W}_{\mathbf{v}, \tilde{\mathbf{r}}}$.

B. Primal Problem and Its Dual

From [15], [16], [18], we re-define (36) to an *equivalent, homogeneous, strengthened* primal problem:

$$\begin{aligned} \min_R f(\tilde{\mathbf{q}}) &= \min_R \tilde{\mathbf{q}}^\top \tilde{\mathbf{Q}} \tilde{\mathbf{q}}, \quad \tilde{\mathbf{q}} = [\text{vec}(\mathbf{R})^\top \ y]^\top \\ \text{s.t. } R^\top R &= y^2 I_3 \\ RR^\top &= y^2 I_3 \\ R^{(i)} \times R^{(j)} &= yR^{(k)}, \quad i, j, k = \text{permute}\{1, 2, 3\} \\ y^2 &= 1. \end{aligned} \quad (37)$$

The primal problem (37) is a QCQP and the corresponding dual problem is defined as

$$L(\tilde{\mathbf{q}}, \boldsymbol{\lambda}) = \gamma + \tilde{\mathbf{q}}^\top (\tilde{\mathbf{Q}} + \tilde{\mathbf{P}}(\boldsymbol{\lambda})) \tilde{\mathbf{q}} = \gamma + \tilde{\mathbf{q}}^\top \mathbf{Z} \tilde{\mathbf{q}}, \quad (38)$$

where \mathbf{P} is the penalization matrix [18]. The Lagrangian relaxation is an unconstrained problem and has a closed-form solution:

$$\begin{aligned} g(\boldsymbol{\lambda}) &= \min_{\tilde{\mathbf{q}}} L(\tilde{\mathbf{q}}, \boldsymbol{\lambda}) = \min_{\tilde{\mathbf{q}}} \gamma + \tilde{\mathbf{q}}^\top \mathbf{Z} \tilde{\mathbf{q}} \\ &= \begin{cases} \gamma, & \text{if } \mathbf{Z} \succeq 0 \\ -\infty, & \text{otherwise.} \end{cases} \end{aligned} \quad (39)$$

Therefore, the maximization of the dual problem (39) is a SDP:

$$g^* = \max_{\boldsymbol{\lambda}} \gamma, \quad \text{s.t. } \mathbf{Z}(\boldsymbol{\lambda}) \succeq 0 \quad (41)$$

This problem is convex and can be solved globally by off-the-shelf specialized solvers [19]. It is shown in [18] that the relaxation is empirically always tight (the duality gap is zero).

APPENDIX C
OBSERVATIONS ON GLOBAL CONVERGENCE AND
CONVEXITY

In this section, we provide numerical results that suggest the proposed method is also applicable to 3D registration problems and may achieve global convergence. Additionally, we show more figures about the potential convexity of (20).

A. Toward Global Convergence of the Proposed Method

We show that the proposed method in the experimental data collected by the *32-Beam Velodyne ULTRA Puck LiDAR* reduces the P2P distance by 68.6%, as shown in Fig. 6. In addition, we illustrate the proposed algorithm can be used in 3D registration problems (point-to-point, point-to-line, point-to-plane) by scaling the simulation (named *Random*) and experimental data (named *RubikCube* and *SpaceStation*) in [17], [18]. The results of the registration problems are shown in Fig. 8 and the experiment setup from [17] is shown in Fig. 9.

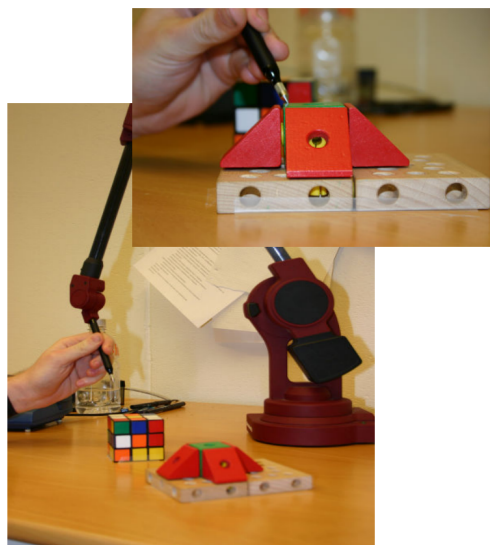


Fig. 9: This figure is taken from [17] to illustrate the experimental setup.

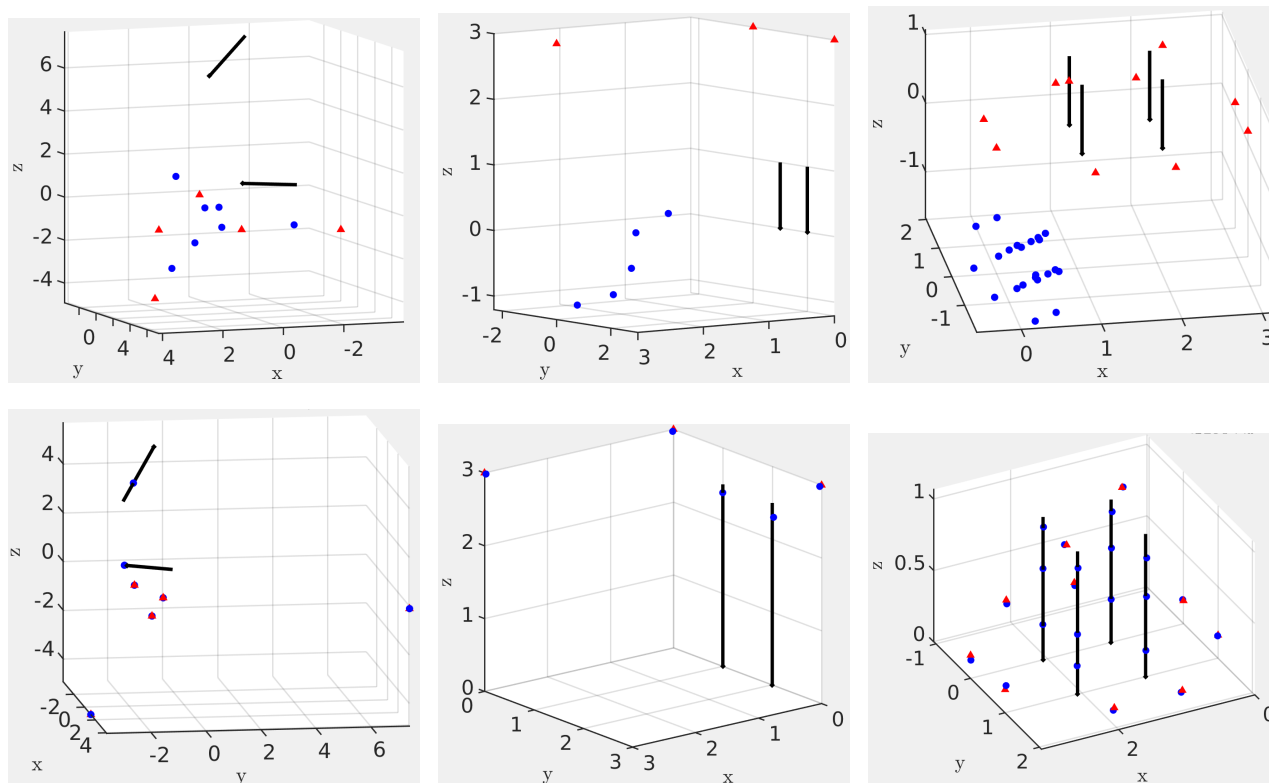


Fig. 8: This figure shows the proposed method can be used in 3D registration problems. The correspondences are point-to-point (marked in blue and red), point-to-line (marked in blue and black), and point-to-plane (not shown to keep the figure readable). The top and bottom row is the initial status and the results of the registration problems, respectively. The simulation (*Random*) with five point-to-point and two point-to-line correspondences are shown in the left column. The result of the experimental data (*RubikCube*) with three point-to-point and two point-to-plane correspondences is shown in the second column. The last column shows the result of the experimental data (*SpaceStation*) with ten point-to-point and 12 point-to-line correspondences.

B. Potential Convexity of $f(s)$ and Bisection Method

Theoretically, a dense search on the scaling s should be performed on a range of interest. However, we have empirically observed that (20) is convex for all of our data sets. Figure 10a shows $f(s)$ is convex for all the sets of the calibration parameters for our LiDAR intrinsic calibration datasets. Similarly, in Fig. 10b shows the convex property of $f(s)$ for the simulation and experimental data in [17], [18]. We, therefore, utilize the bisection method to determine the scaling s . It is emphasized that the convexity of (20) is unknown at this time.

Let ${}^L_k s$ and ${}^U_k s$ be the lower and upper bounds of the scaling parameters at the k -th iteration. Let ${}_{k+1}s = ({}^U_k s + {}^L_k s)/2$ be the update for $(k+1)$ -th iteration. The updates of the scaling parameters are defined as:

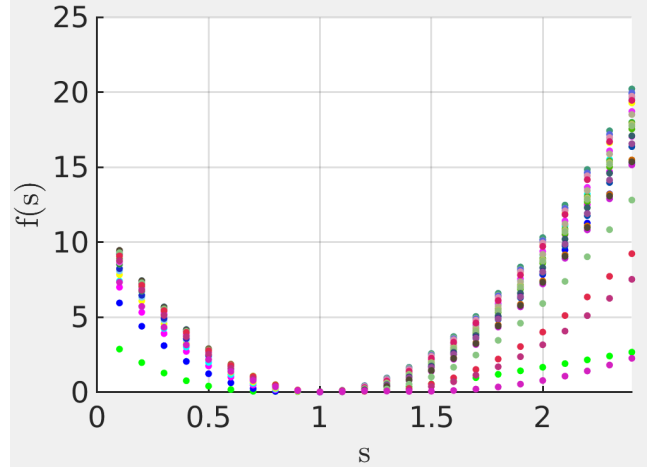
$$\begin{aligned} {}^L_{k+1}s &= \begin{cases} {}_{k+1}s, & \text{if } \nabla f({}_{k+1}s) < -\epsilon \\ {}^L_k s, & \text{otherwise} \end{cases} \\ {}^U_{k+1}s &= \begin{cases} {}_{k+1}s, & \text{if } \nabla f({}_{k+1}s) > \epsilon \\ {}^U_k s, & \text{otherwise} \end{cases}, \end{aligned} \quad (42)$$

where the symmetric difference is used to approximate $\nabla f({}_{k+1}s)$:

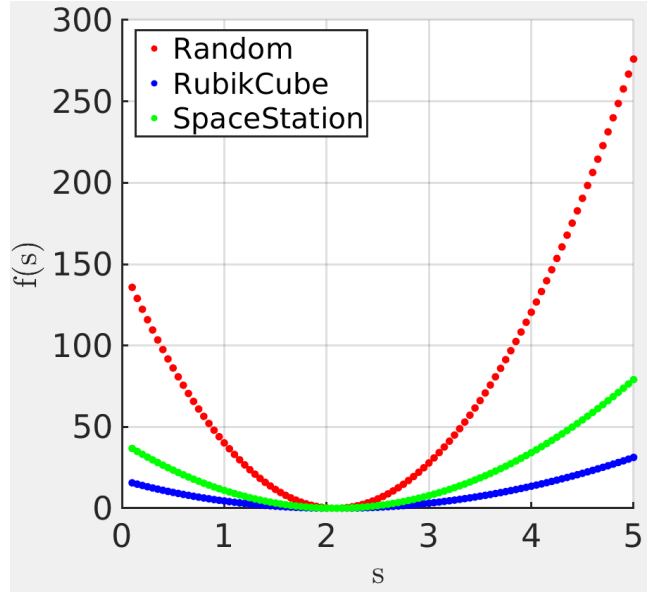
$$\nabla f({}_{k+1}s) \approx \frac{f({}_{k+1}s + h) - f({}_{k+1}s - h)}{2h}, \quad (43)$$

where $h > 0$ is a small value (taken as 10^{-3}).

Remark 12. To obtain more accurate results, $\mathbf{R}({}_{k+1}s + h)$, $\mathbf{v}({}_{k+1}s + h)$, $\mathbf{R}({}_{k+1}s - h)$ and $\mathbf{v}({}_{k+1}s - h)$ should be computed separately.



(a)



(b)

Fig. 10: This figure shows f vs s for the calibration parameters. The top figure shows the calibration parameters for all the rings, for f defined in (20). The bottom figure show f for the 3D registration problems (point-to-point, point-to-line, point-to-plane). We suspect that the convex shape seen in the plot is true in general. On going work is seeking a proof.